Renewable Energy 203 (2023) 664–676

Contents lists available at ScienceDirect

Renewable Energy

journal homepage: www.elsevier.com/locate/renene

Cold energy storage as a solution for year-round renewable artificial ground freezing: Case study of the Giant Mine Remediation Project

Ahmad F. Zueter, Agus P. Sasmito *

Department of Mining and Materials Engineering, McGill University, 3450 University, Frank Dawson Adams Bldg., Montreal, QC H3A0E8, Canada

A R T I C L E I N F O

Keywords:
Cold energy storage
Thermosyphon
Artificial ground freezing
Energy saving
Permafrost protection
Giant Mine

A B S T R A C T

In cold regions, passive thermosyphons are often employed in permafrost protection and artificial ground freezing (AGF) applications. While passive thermosyphons utilize available cold wind during cold seasons, energy-intensive refrigeration plants are sometimes needed to run thermosyphons in warmer seasons. In this study, a novel cold energy storage (CES) concept is proposed to operate thermosyphons year-round using renewable energy resources. The proposed system is based on additional energy storage ground coupled thermosyphons (ST) and heat extraction pipes (HEP). In cold seasons, the STs store wind cold energy, which is then transferred in warmer seasons using HEPs to the site of interest. The system is mathematically demonstrated using numerical models validated in our previous work against field data from the Giant Mine Remediation Project (GMRP). The results reveal that the proposed system enhances the heat extraction capacity of primary thermosyphons (located in the site of interest) by more than 15%. Further, the ground freezing process is achieved one year faster. Overall, this study presents the foundation of an innovative concept that can help run thermosyphons using renewable resources in cold regions, especially at the GMRP.

1. Introduction

The Giant Mine was a major economic force of the Northwest Territories (NT), producing 7 million ozt of gold over the second half of the twentieth century [1,2]. Despite these economic benefits, gold mining created a massive environmental burden amounting for 237,000 tons of a lethal byproduct called arsenic, which has been stored in underground chambers [1]. Arsenic leakage poses several environmental and social catastrophes. The mine waste is situated along the shoreline of Yellowknife Bay on Great Slave Lake, one of the largest freshwater bodies in Canada. Arsenic concentration in Yellowknife Bay is five times higher than that of drinkable water [3], influencing the fish habitat. The Dettah First Nation people, who are closest to the mine, are severely affected by this catastrophe as they cannot safely practice hunting and fishing in the vicinity — not to mention the demise and health issues in the 1950s due to arsenic consumption [4]. To mitigate the impact of arsenic leakage, the Canadian Government initiated the Giant Mine Remediation Project (GMRP) in collaboration with the Yellowknives Dene First Nation. Among various containment methods, a reliable one called the frozen block was selected, where the environmental waste is encapsulated in a frozen shell. To this end, artificial ground freezing (AGF) systems will be indefinitely employed. Nonetheless, active AGF approaches can result in huge economic and environmental costs; a set of 150 hybrid thermosyphons, that may employ refrigeration plants in summer seasons, could annually consume around 3.5 GWh [5] and correspondingly produce substantial greenhouse gas emissions [6]. The energy expenditures and greenhouse gas emissions of refrigeration can amount for 1-5% of the provincial ones [6]. Accordingly, a novel AGF method based on renewable energy is needed to securely contain environmental waste of the GMRP while substantially reducing the environmental and economic costs.

Thermosyphons are common devices in artificial ground freezing applications, ranging from support of civil structures (roads, buildings, etc.) to containment of contaminated areas. The main role of thermosyphons is transferring thermal energy from the ground to a colder heat sink (cold wind or refrigerated coolant) to freeze the ground, thus increasing the ground strength and impermeability. Especially in cold regions such as the NT, thermosyphon technologies are widely used in the AGF industry due to their ability to passively transfer cold energy from the winter wind to the ground. While passive cooling of thermosyphons is sufficient in some applications, active refrigeration techniques are sometimes combined with passive thermosyphons to maintain heat extraction from the ground in summer seasons. For instance, hybrid thermosyphons, which combine passive and active cooling methods, have been used in the construction of the Diavik Mine dams and dikes [7], as well as the containment of hazardous

* Corresponding author.
E-mail address: agus.sasmito@mcgill.ca (A.P. Sasmito).

https://doi.org/10.1016/j.renene.2022.12.093
Received 19 May 2022; Received in revised form 5 December 2022; Accepted 24 December 2022
Available online 29 December 2022

Nomenclature

Latin letters

A	Area [m^2]
c_p	Specific heat capacity [J kg^{-1} K^{-1}]
f	Friction factor [–]
h	Convective heat transfer coefficient [W m^{-2} K^{-1}]
h_{fg}	Specific latent heat of evaporation [J kg^{-1}]
k	Thermal conductivity [W m^{-1} K^{-1}]
L	Specific latent heat of fusion [J kg^{-1}]
$\dot{m}$	Mass flow rate [kg s^{-1}]
Nu	Nusselt number [–]
Pr	Prandtl number [–]
q	Heat flux [W m^{-2}]
R	Thermal resistance [K W^{-1}]
Re	Reynolds number [–]
T	Temperature [K]
t	Time [s]
z	Depth, where $z = 0$ at ground surface [m]

Greek letters

δ	Frozen ground radius [m]
γ	Liquid fraction [–]
μ	Viscosity [Pa s]
ϕ	Porosity [–]
ρ	Density [kg m^{-3}]
τ	Active operation period per year [s]

Subscripts

a	Air
atm	Atmospheric
e	Evaporator
f	Liquid state
g	Gas state
HTF	Heat transfer fluid
i	Inner wall
n	Condenser
o	Outer wall
s	Saturation state
w	Water, in its frozen or unfrozen states

waste at the Oak Ridge National Project [8]. In other applications featuring hybrid cooling methods, active freeze-pipes are initially installed in ground boreholes to accelerate the formation of the frozen ground by passing a refrigerated coolant through the pipes. Once the desired frozen ground is formed, active pipes are removed, and a passive/hybrid thermosyphon is installed to reduce the cooling load especially during cold seasons. Such active followed by passive refrigeration system has been installed to support the foundations of the Kuparuk River Module Crossing in Russia [9] and is also proposed for the GMRP. Overall, active refrigeration plants can increase the system reliability and heat extraction capacity; however, they require intensive energy resources.

Consequently, several studies have been conducted to passively enhance the heat extraction capacity of thermosyphons either by (1) integrating other static components to the ground or (2) improving the design of thermosyphons. Guo et al. [10] observed that vegetation cover effectively insulates the ground in warm seasons thus reducing cold energy dissipation. Xu et al. [11] and Varmalov et al. [12] demonstrated that integrating artificial insulation boards can further preserve the cold energy in the ground. In attempts to enhance the insulation, Zhou et al. [13] proposed a tri-layered asphalt pavement that feature a decreasing thermal conductivity from top to bottom. On the other hand, Zhong et al. [14] developed new asphalt mixture that decreases its thermal conductivity while maintaining its strength. Despite the benefits of insulation boards, several studies reported that crushed rock revetments have to be integrated as well to better preserve the ground's cold energy [15–18].

Other studies focused on improving the thermosyphon geometry as well as thermosyphons layout to enhance their heat extraction capacity. Lyazgin et al. [19] increased the daily operational hours of thermosyphons by manufacturing the thermosyphon vessel from aluminum alloys (instead of traditional steel vessels) due to its high thermal conductivity. Bayasan et al. [20] increased the heat extraction capacity of the condensers by adding secondary fins on primary fins. Zhang et al. [21] proposed employing a nanofluid of favourable thermal conductivity as the working fluid inside the thermosyphon to decrease its thermal resistance. In another attempt to decrease the thermal resistance inside the thermosyphon, Solomon et al. [22] proposed using a grooved heat pipe to accelerate the evaporation/condensation cycle. In regards to the evaporator section, Tian et al. [23] observed that inclined evaporators are preferred due to their ability to maintain a uniform temperature (frozen front) below highway embankments. Kukkapalli et al. [24,25] designed T-shape and Y-shape, in addition to tree-like T-shape and Y-shape, evaporators; the numerical analysis revealed that the thermal performance of these designs is preferable over the traditional type of L-shaped thermosyphons. Pei et al. [26] suggested using adjustable evaporator section to tune the ground temperature profile. Further, Pei et al. [27,28], Chang et al. [29], and Chen et al. [30] proposed alternating thermosyphons layout across Qinghai–Tibet Roadway to enhance the frozen front profile.

While hybrid thermosyphons utilizing active refrigeration plants have been studied in the literature [5,31,32], limited number of studies considered running thermosyphons in warm seasons using sustainable energy resources. Wagner et al. [33] recently proposed using solar panels to run mechanical refrigeration for hybrid thermosyphons, especially in remote areas not connected to the national grid. Alzoubi et al. [34,35] conducted mathematical analysis confirming the high potential of the cold energy storage concept to run the ground freezing process indefinitely. However, the mathematical model did not consider the cold energy storage medium.

In this study, an innovative cold energy storage (CES) concept is proposed to run thermosyphons during warm seasons as well as cold ones. In our proposed system, several thermosyphons are used to store cold energy in the ground during cold seasons. In warm seasons, the cold energy is extracted and directed towards application of interest. Conjugate numerical model of thermosyphons derived in our previous work is employed and adapted to simulate our CES concept. The model has been validated against GMRP field data and a well-controlled experimental study conducted by Pei et al. [36]. The proposed cold energy storage concept is then examined for the case of the GMRP. The impact of operational parameters on the CES system is also addressed.

2. Methodology

In this study, a CES concept is proposed to allow thermosyphons to run year-round using renewable energy resources. The conceptual methodology will be firstly described followed by the mathematical one.

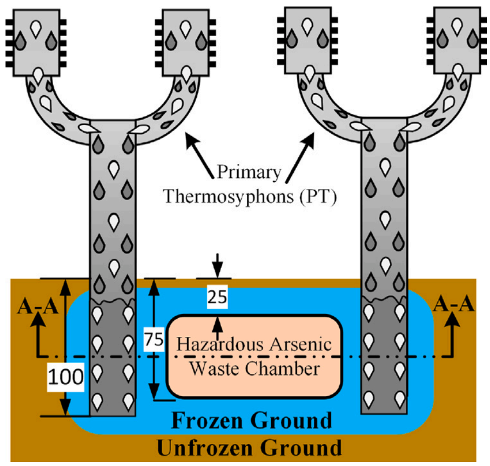

Fig. 1. Arsenic containment at the Giant Mine Remediation Project using thermosyphons (not to scale).

2.1. Conceptual methodology

At the GMRP, several 100 m deep thermosyphons operate next to each other to encapsulate arsenic chambers extending from 25 m to 75 m below the ground surface, as shown in Figs. 1 and 2(a-2). In this study, an innovative cold energy storage concept is developed to allow thermosyphons to run passively year-round for the case of the GMRP in particular and other permafrost protection applications in general.

In our proposed system, There are two sets of thermosyphons working simultaneously: (1) Primary thermosyphons (PT), operating in the site of interest, which is the GMRP in this study, as shown in Fig. 2(a-2) and (2) storage thermosyphons (ST), as shown in Fig. 2(a-1). In winter seasons, PTs extract heat from the ground to freeze zones of interest, as shown in Fig. 2(b-2). Concurrently, STs store cold energy, as shown in Fig. 2(b-1), in a nearby location. In warm seasons, the finned sections of the PTs and STs become idle due to the absence of cold wind. To keep PTs active, the cold energy stored by the STs is then transferred to the PTs, as shown in Fig. 2(c-1,c-2). Particularly, a HTF passes through a heat extraction pipe (HEP), extracts the stored cold energy, and then transfers the cold energy to the PT through a helical coil acting as a secondary condenser.

In practical field scenarios, a single thermosyphon is not sufficient to freeze the ground of large scale applications such as the GMRP. Instead, several PTs operate next to each other, as can be seen from Fig. 2(b-2). Consequently, there is a need for several STs to provide enough cold energy. Thus, an important parameter of interest for performance optimization is the spacing between the PTs as well as the STs. This study will focus more on the CES concept; accordingly, the effect STs spacing will be examined. Throughout this study, the number of PTs is set to be equal to the number of STs; thus, each ST provides cold energy for one PT.

2.2. Mathematical methodology

In this subsection, the mathematical model used to demonstrate our idea is presented.

2.2.1. Governing equations

A porous ground occupying the GMRP area is considered as the computational domain of the present study. The local thermal equilibrium (LTE) assumption [37] is valid as shown by Zueter et al. [38]. Energy balance in the ground can thus be expressed as

$$\frac{\partial(\overline{\rho c_p} T)}{\partial t} = \nabla \cdot (\overline{k} \nabla T) + S, \tag{1}$$

where $\overline{\rho c_p}$ and $\overline{k}$ are the equivalent heat capacity and thermal conductivity of the ground (rock and water), while the source term, S, represents the latent of the water content as

$$S = -\frac{\partial(\gamma \overline{\rho L})}{\partial t}, \tag{2}$$

where $\overline{\rho L}$ is the ground volumetric latent heat related to the ground porosity as

$$\overline{\rho L} = \phi \rho_w L_w, \tag{3}$$

where ρ_w and L_w are the density and latent heat of water, respectively. γ is the liquid fraction of the water content defined as a function of the water liquidus temperature T_{liq} and solidus temperature T_{sol} as

$$\gamma = \begin{cases} 0 & , T < T_{sol}; \\ \frac{T - T_{sol}}{T_{liq} - T_{sol}} & , T_{sol} \leq T \leq T_{liq}; \\ 1 & , T > T_{liq}, \end{cases} \tag{4}$$

2.2.2. Boundary conditions

Along the bottom boundary, geothermal heat flux is set as [39]

$$-\overline{k} \frac{\partial T}{\partial n}\bigg|_{bottom\ boundary} = q_{geo}, \tag{5}$$

where q_{geo} = 0.06 [W/m^2]. At the side boundary which represents the middle distance between two thermosyphon, thermal symmetry is considered as

$$\frac{\partial T}{\partial n}\bigg|_{side\ boundary} = 0. \tag{6}$$

The top boundary of field simulations is subject to atmospheric convection as

$$-\overline{k} \frac{\partial T}{\partial n}\bigg|_{top\ boundary} = h_{atm}(T|_{top\ boundary} - T_a), \tag{7}$$

where T_a is the air temperature and the atmospheric heat transfer coefficient, h_{atm} is set at 3 [W/(m^{2}K)].

As for the thermosyphon modeling, Zueter et al. [40] revealed that deep thermosyphons such as those installed at the GMRP can exhibit a unique boiling profile. However, in this study, we use a reseanably accuerate thermal-resistance-network model derived and validated in our previous work [5]. The thermosyphon boundary is coupled to the ambient air temperature or helical coil temperature as

$$q_e = \frac{Q_{total}}{A_e} = \frac{T_\infty - T_e}{R_{eq} A_e} = -\overline{k} \frac{\partial T}{\partial n}\bigg|_e, \tag{8}$$

where subscript e denotes the evaporator section. The equivalent thermal resistance, R_{eq}, is determined following a thermal network model explained in Fig. 3. Various Nusselt correlations were employed to determine each thermal resistance as

$$R = \frac{1}{hA} \tag{9}$$

where h is the heat transfer coefficient and A is the heat transfer area. Starting at the evaporator, Imura's correlation [41] is employed to determine the heat transfer coefficient of boiling as

$$h_{2,3} = 0.32 \left[\frac{\rho_f^{0.65} k_f^{0.3} c_{p,f}^{0.7} g^{0.2} q_e^{0.4}}{\rho_g^{0.25} h_{fg}^{0.4} \mu_f^{0.1}} \right] \left(\frac{P_s}{P_{atm}} \right)^{0.3} \tag{10}$$

where the thermophysical properties of CO_2 can be found in Table 2. The condensation heat transfer coefficient is modelled using the Nusselt theory as [42]

$$h_4 = 0.925 \left[\frac{k_f^3 \rho_f^2 g h_{fg}}{\mu_f q_n \ell_n} \right]^{1/3}. \tag{11}$$

where q_n is the heat flux through the condenser while L_n is the length of the condenser. The ground heat is eventually extracted by cold wind

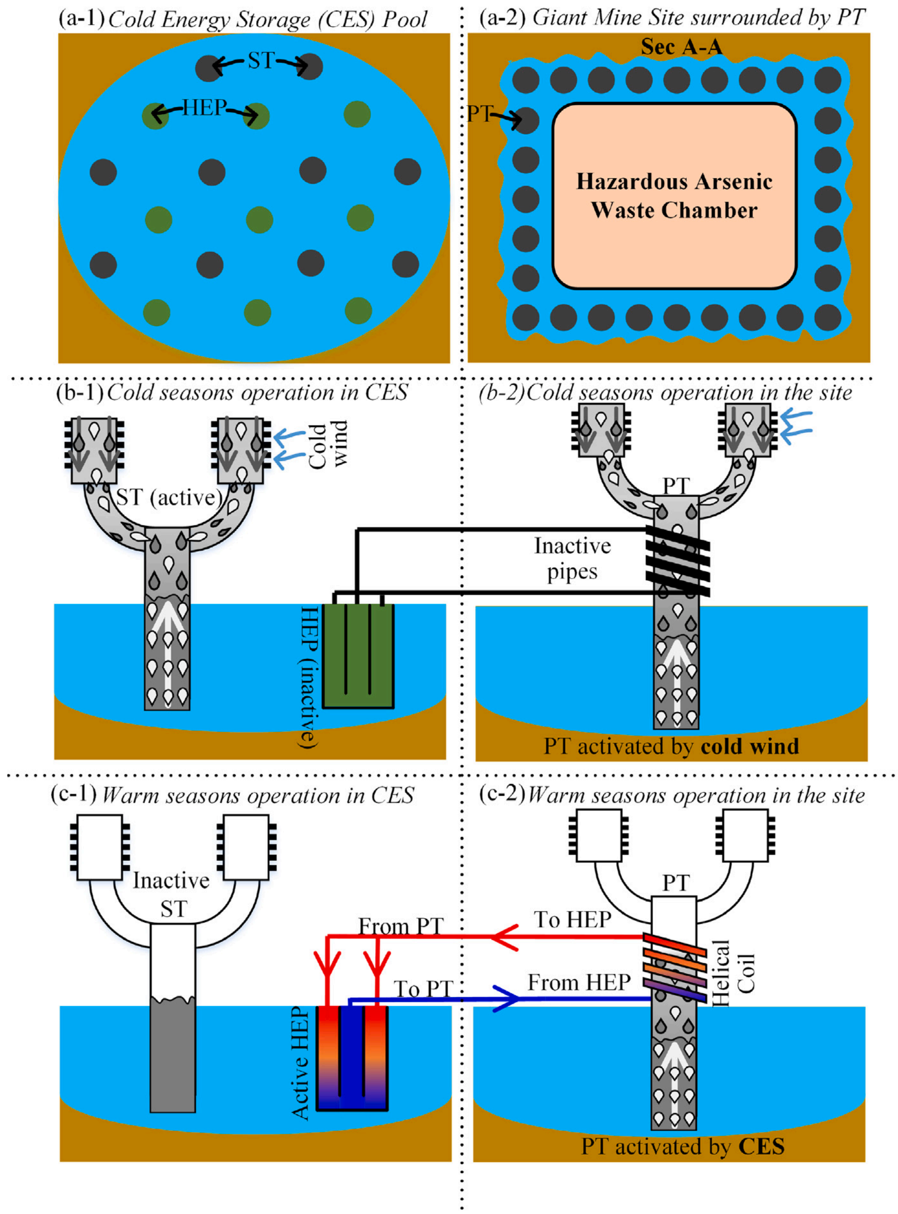

Fig. 2. Illustration of the conceptual methodology of the present study: (a-1) Top view of the cold energy storage (CES) pool showing the storage thermosyphons (ST) and heat extraction pipes (HEP) arranged in a diamond configuration, (a-2) horizontal cross-sectional view of primary thermosyphons (PT) encapsulating the arsenic chambers (refer to Fig. 1 to see the position of A-A section), (b-1) charging operational mode of CES during cold seasons, (b-2) the operation of PT in cold seasons utilizing cold wind, (c-1) discharging operation mode of CES, and (c-2) the operation of PT in our proposed CES system in warm seasons using stored cold energy.

or chilled coolant from the CES pool. The Nusselt number is modelled based on the Reynolds number, Re_a, as [39,43]

$$Nu_a = \frac{h_6 D_{o,n}}{k_a} = \begin{cases} \eta_{fin}\ 0.989 Re_a^{0.330} Pr_a^{1/3} & , Re_a < 4; \\ \eta_{fin}\ 0.911 Re_a^{0.385} Pr_a^{1/3} & , 4 \le Re_a < 40; \\ \eta_{fin}\ 0.683 Re_a^{0.466} Pr_a^{1/3} & , 40 \le Re_a < 4000; \\ \eta_{fin}\ 0.193 Re_a^{0.618} Pr_a^{1/3} & , 4000 \le Re_a < 40000; \\ \eta_{fin}\ 0.027 Re_a^{0.805} Pr_a^{1/3} & , 40000 \le Re_a, \end{cases} \tag{12}$$

where $D_{o,n}$ is the characteristic length of wind flow equivalent to the outer diameter of condenser wall and η_{fin} is fin efficiency set at 65% based on the fin geometry as per charts of Gardner [39,44] for circular fins. Finally, the Nusselt number of the HTF flow across the helical coil is calculated based on Seban and Mclanghin correlation [45,46] as

$$Nu = \frac{h_7 D_{HTF}}{k_{HTF}} = 0.065 f_{HTF}^{0.33} Re_{HTF}^{0.66} Pr_{HTF}^{0.33}, \tag{13}$$

where the characteristic length for calculating the Reynolds number is inner diameter of the coil and f_c is the friction factor of the HTF calculated as [47]

$$f_{HTF} = \frac{64}{Re_{HTF}} \left\{ 1 - \left[1 - \left(\frac{11.6}{Dn_{HTF}} \right) \right]^{0.45} \right\}^{-1} \tag{14}$$

where Dn_{HTF} is the Deans number. The switches S_2 and S_3 are actively controlled by the specified operational duration for CES and passive cooling. On the other hand, the S_1 switch inside the thermosyphon is added to deactivate the thermosyphon when the natural convection cycle stops due to lower evaporator temperature than condenser temperature. More detailed description and evaluation of the thermal resistance network can be found in our previous work [5].

In order to quantify the amount of heat extracted by HEPs, the axial HTF temperature, $T_{HTF}(z)$, is correlated to the ground through

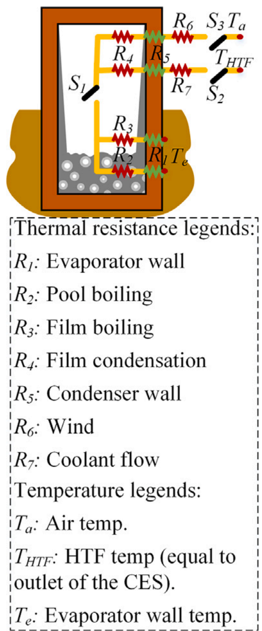

Fig. 3. Thermal resistance network model of thermosyphons.

a convective boundary condition as

$$q_{HEP}(z) = -\bar{k}\frac{\partial T(z)}{\partial n}\bigg|_{o,w} = h(z)\Big[T(z)|_{o,w} - T_{HTF}(z)\Big], \tag{15}$$

where the HTF temperature evolution is monitored using a space marching algorithm based on the first law of thermodynamics as

$$\Delta T_{HTF}(z) = \frac{q_{HEP}(z)}{\dot{m}_{HTF}c_{p,HTF}}, \tag{16}$$

where $T_{htf}(z = 0)$ and $T_{htf}(z = L)$ correspond to the HTF inlet and outlet temperatures, respectively. To evaluate the heat transfer coefficient, a tabulated analytical solution of Shah [48] are employed for laminar annular flow. All details on the evaluation of the heat transfer coefficient and space marching algorithm can be obtained from our previous work [49,50]. The adopted algorithm demonstrates high computational effeciency even in conducting thousands of Monte-Carlo simulations. [51]. The total amount of heat extracted by HEP can be determined based on the inlet and outlet temperatures of the HTF as

$$\dot{Q}_{HEP} = \dot{m}_{HTF}c_{p,HTF}\Big(T_{HTF}(z = L) - T_{HTF}(z = 0)\Big) \tag{17}$$

Throughout this study, the initial temperature of the ground is set according to geothermal temperature gradient recorded in the field approximated by the following correlation:

$$T_{initial}[K] = 278.8e^{-c_1} + 4.065 \times 10^{13}\ e^{-c_2} \tag{18}$$

where $c_1 = \left(\frac{z[m]-351.1}{2292}\right)^2$, $c_2 = \left(\frac{z[m]+754.7}{133.4}\right)^2$, and z is the depth from ground surface.

2.3. Choice of numerical parameters

Second-order upwind schemes were selected to discretize the spatial and transient terms of the governing equation of the ground (Eq. (1)). ANSYS Fluent 18.1 was used to compute the equations as prescribed by our model and user-defined functions. Mesh independence study and time-step independence study were conducted and ensured. The selected mesh size and type greatly relies on the simulation scenario as we have conducted various 3D simulations of different length scales. In all cases, the mesh and geometry were generated with the aid of ANSYS Fluent 18.1. The mathematical methodology has been validated against field data in our previous work [5].

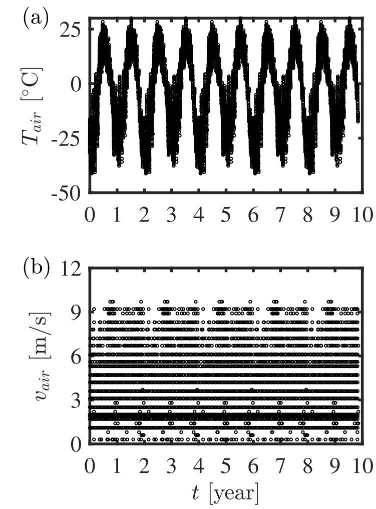

Fig. 4. Hourly air data measured by the Giant Mine weather station [52]: (a) air temperature data and (b) wind speed data.

Table 1
Geometry of thermosyphons used in this study. The coil geometry is applicable to PTs only (there is no coil attached to STs).

Property	Value
Finned area of passive condenser	39 [m^2]
Thermosyphon outer diameter	0.114 [m]
Thermosyphon thickness	6 [mm]
Helical coil outer diameter	10.3 [mm]
Helical coil thickness	1.7 [mm]
Helical coil height	2.4 [m]

3. Results and discussion

This section is divided into three main subsections. First, we will examine the capacity of a single thermosyphon to store cold energy in the ground. Second, a pool of STs will be modelled independently to examine how the storage capacity is affected when multiple STs are installed. Finally, a coupled model that links heat extraction of PTs with STs is simulated. Throughout this section, hourly weather data as measured by the Giant Mine Weather Station is used as per Fig. 4.

3.1. Maximum storage capacity of a single thermosyphon

In this section, we evaluate the maximum energy that can be stored by a single thermosyphon installed near the GMRP site to serve as a workbench for the upcoming discussion on the results. Accordingly, a single thermosyphon was modelled over ten years of similar geometry to those installed at the GMRP as per Table 1. In order to evaluate the maximum energy stored by a single thermosyphon, the outer boundaries of the computational domain, r_o, are gradually increased until the model becomes independent from the distance between the thermosyphon and the outer boundaries.

By increasing the distance between the thermosyphon and outer boundaries gradually, a boundary independent solution is obtained at a distance of around 15 m, as shown in Fig. 5. Evidently, as the distance increases, the stored energy becomes larger due to the higher thermal capacity of the ground at larger volumes. Nevertheless, at a distance of around 15 m, the stored energy is purely dominated by the capacity of energy extraction by the cold wind rather than ground volume. The intermittent increase of stored energy is attributed to the seasonal weather conditions. In winter seasons, the air temperature is low enough to run the thermosyphon thus increasing the amount of cold energy stored. On the other hand, the thermosyphon becomes idle during warm seasons leading to a dormant period interrupting the heat extraction process.

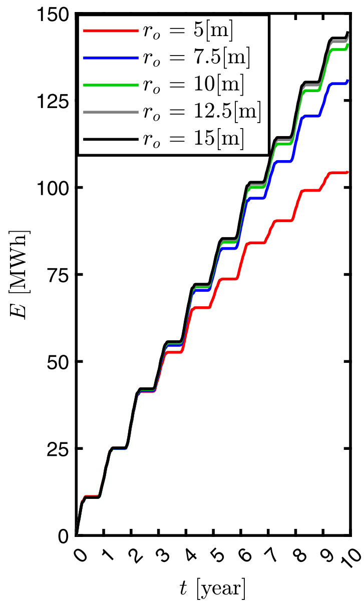

Fig. 5. Maximum energy stored by a single thermosyphon operating independently is estimated at 150 [MWh] over 10 years.

3.2. Energy stored by several adjacent thermosyphons

In practical field scenarios, a single ST cannot store sufficient energy especially for grand applications such as the GMRP. Consequently, instead of installing a single ST, several thermosyphons should be installed next to each other to increase the amount of cold energy stored.

Table 2
Thermophysical properties of CO_2, the working fluid inside thermosyphons, and bedrock of the Giant Mine site. The water content is 1%.

Material	ρ [kg/m^3]	c_p [J/(kg k)]	k [W/(m k)]	μ [Pa s]
Condensate CO_2 [53]	959	2396	0.117	1.09E−4
Vapour CO_2 [53]	81.9	1643	18.0E−2	1.42E−5
Frozen rock [54]	2926	814	3.45	–
Unfrozen rock [54]	2927	822	3.44	–

The cold energy of thermosyphons is extracted by a heat extraction pipe (HEP), as shown in Fig. 2(c-1). In this study, a 30% calcium chloride solution is considered due its thermal stability as well as industrial reliability in the field (e.g., AGF of the Cigar Lake Uranium Mine [49,50]). Also, the ST and HEP are arranged in a diamond configuration shaped as a bilateral right-angle triangle as shown in Fig. 2(a-1). The length of each of the bilateral sides is denoted d.

While there are several geometrical parameters that can be extensively studied and optimized, this study aims at demonstrating the concept of cold energy storage. Three main operational parameters are highlighted in this subsection: (1) The distance between the ST and HEP (d), (2) the volume flow rate of the heat transfer fluid (VF), and (3) the inlet temperature of the HTF (T_{in}).

3.2.1. Effect of distance between ST and HEP

As noted in Section 3.1, the larger the ground in vicinity of a thermosyphon, the higher the thermal storage capacity. Nevertheless, to effectively extract cold energy through HEP, sufficient amount of cold energy should travel the distance between the HEP and ST. Accordingly, the distance has been varied from 1 to 3 m to better estimate the optimum spacing resulting in highest heat extraction for the case of the GMRP.

The parametric analysis shows that the amount of cold energy stored is proportional to d, as shown in Fig. 6(a). The *added benefit* of

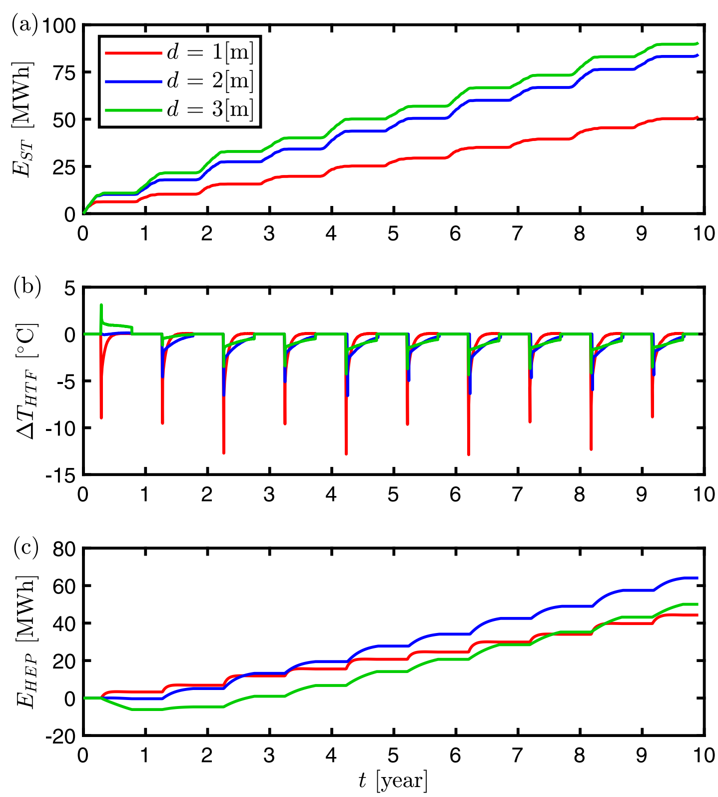

Fig. 6. Effect of spacing between ST and HEP on the (a) amount of energy stored by each ST, (b) temperature difference across the HTF outlet and inlet to the CES, $\Delta T_{HTF} = T_{HTF,outlet} - T_{HTF,inlet}$, and (c) amount of energy extracted by each HEP ($T_{in} = -5°$[C] and $VF = 1$ [m^3/h]).

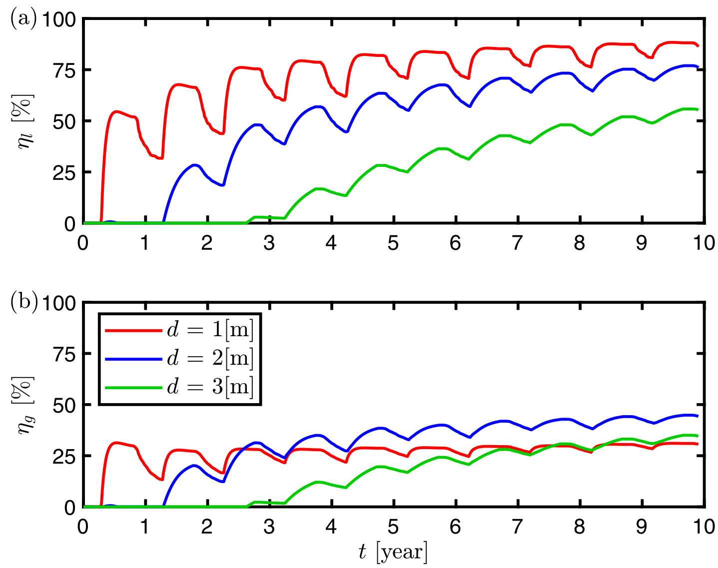

Fig. 7. Effect of spacing between ST and HEP on the (a) local efficiency (η_l) and (b) global efficiency (η_g).

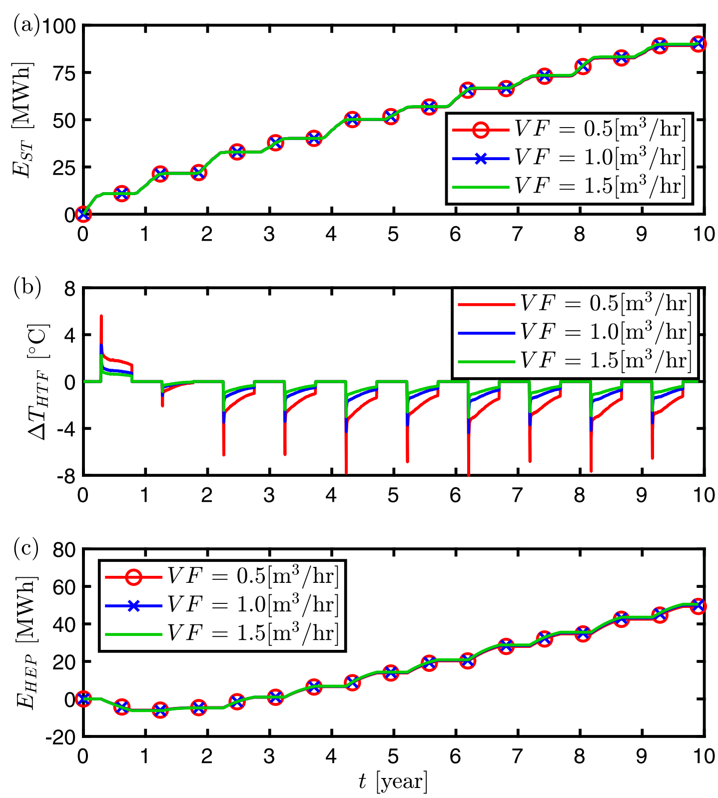

Fig. 8. Effect of the volume flow rate of the HTF on the (a) amount of energy stored by each ST, (b) temperature difference between the HTF inlet and outlet, and (c) amount of energy extracted by each HEP ($d = 1$ [m] and $T_{in} = -5$[°C]).

increasing d however decreases as d increases. For instance, increasing d from 1 [m] to 2 [m] results in an increase in stored energy by around 30 [MWh] after 10 years (for each single ST and HEP); on the other hand, increasing d, from 2 [m] to 3 [m] increases the energy stored by only 7 [MWh] after the same time.

While larger ground volume has the capacity of storing more energy, the amount of energy extracted highly depends on how close the HEP to the ST as well, as can be seen from Fig. 6(b,c). In the short term, a closer distance is desired since less time is needed for cold energy to march from the ST to HEP. After the first winter, cold energy is only extracted when $d = 1$ [m]. At higher d, positive temperature difference is observed between the inlet and outlet of HTF, implying that the HTF extracted *hot* energy (as in goethermal energy extraction applications using HEP [55,56]), which is undesirable in cold energy storage for AGF applications. It takes 1 winter and 2 winters for cold energy to be extracted at $d = 2$ [m] and $d = 3$ [m], respectively. Despite that, the cold energy extracted in the case of $d = 2$ [m] becomes higher than that of $d = 1$ [m] after around 3 winters, due to the higher amount of cold energy stored in the former.

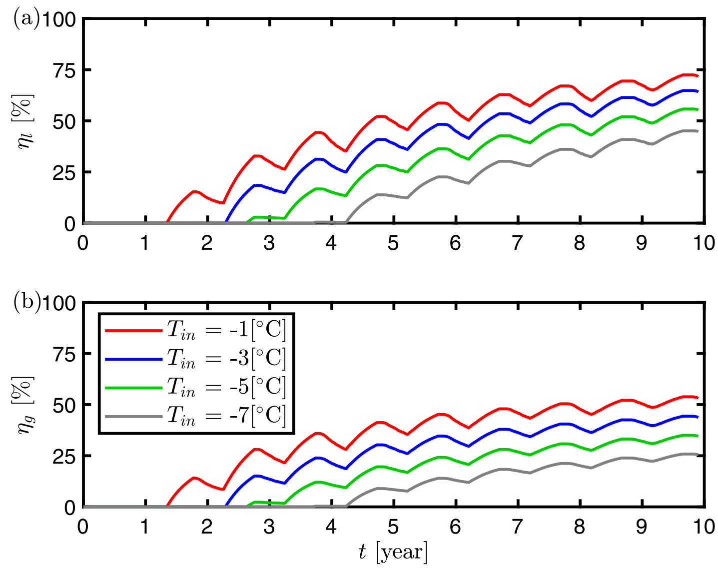

Fig. 9. Effect of HTF inlet temperature on the (a) local efficiency (η_l) and (b) global efficiency (η_g) - $d = 2$ [m] and $VF = 1$ [m^3/h].

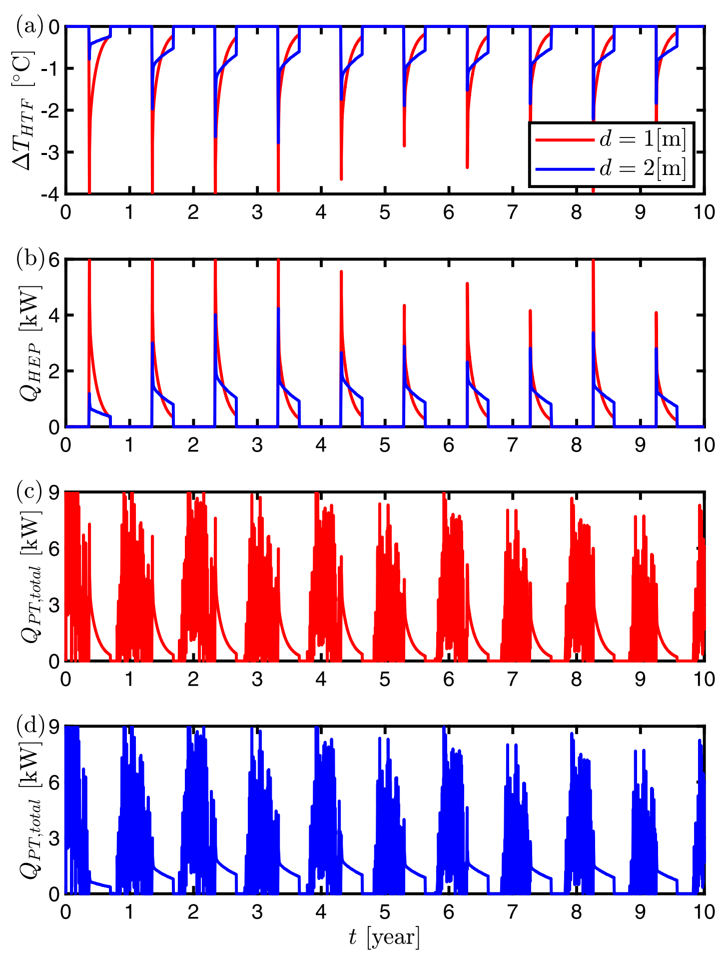

Fig. 10. Effect of d when the discharging period is four months: (a) Temperature difference of the HTF across the HEP, (b) rate of cold energy extracted by each HEP, (c) rate of energy extracted by each PT when $d = 1$ m, and (d) rate of energy extracted by each PT when $d = 2$ m.

To better understand the difference in performance at different d, the concepts of local efficiency, η_l, and global efficiency, η_g, are introduced. The local efficiency is defined as the amount of energy extracted by HEP, E_{HEP}, divided by the amount of energy stored by ST, E_{ST}, ($\eta_l = E_{HEP}/E_{ST}$) in the *same* system. On the other hand, η_g compares E_{HEP} to the maximum energy that can be stored by a single

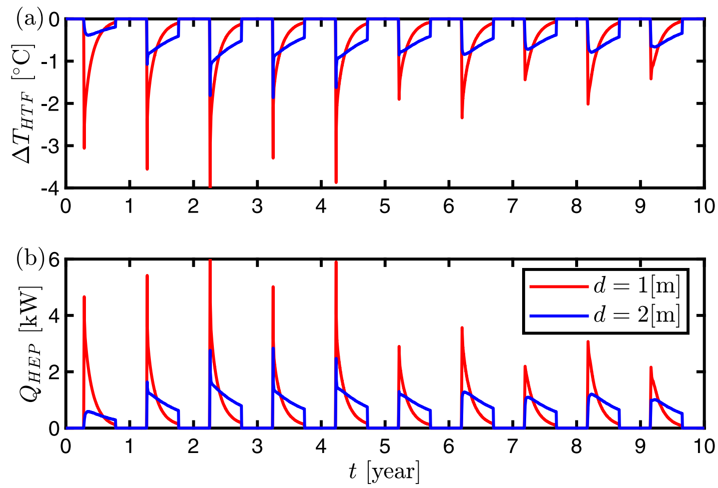

Fig. 11. Effect of d when the discharging period is six months: (a) HTF temperature difference at the CES and (b) heat-rate extracted by each HEP.

thermosyphon shown in Fig. 5 ($\eta_g = E_e/E_{max}$). The results reveal that η_l is inversely proportional to d, as can be deduced from Fig. 7(a). This implies that most energy stored is extracted at lower d. In the case of d = 1 [m], 85% of the energy stored is extracted after 10 years, as compared to 75% and 55% at d = 2 [m] and d = 3 [m], respectively.

Since higher local efficiency does not necessarily imply higher heat extraction, the concept of global efficiency is introduced where the maximum energy that can be stored by a single thermosyphon is used as a reference. In a similar trend of Fig. 6(c), d = 1 [m] provides best performance in the short term, but d = 2 [m] is preferred between the second and tenth years of operation. The global efficiency at d = 1 [m] quickly reaches a semi-steady state at 28% indicating that the system already extracts maximum amount possible of cold energy stored in every winter. In other words, the maximum global efficiency at d = 1 [m] is 28%. The case of d = 2 [m] is approaching the same behaviour after 10 years at $\eta_g \sim 50\%$. When d = 3 [m], the global efficiency is progressively increasing and will be higher than other cases after longer periods.

Overall, the spacing should be determined based on the desired payback period; shorter spacing can result in faster payback but less cold energy in the long run, and vice-versa. Thus, when implementing the concept of cold energy storage, it might be desired to alternate d to compromise between the speed of the payback as well the long-term cold energy stored.

3.2.2. Effect of HTF volume flow rate

The volume flow rate, VF, of the HTF is an essential operational design parameter in energy systems. Thus, the VF was changed in this subsection from 0.5[m^3/h] to 1.5[m^3/h]. The results show that the amount of energy stored by ST is similar regardless of the volume flow rate. This is attributed to the same spacing between HEPs and STs (equal d) as well as same atmospheric conditions, as noted in Fig. 8(a). Nonetheless, the temperature difference between the inlet and outlet of the HTF, ΔT_{HTF}, is highly affected by the volume flow rate; particularly, lower flow rate results in higher temperature difference, as can be seen in Fig. 8(b). The volume flow rate of the HTF can thus be controlled to ensure the chemical and thermal stability of the HTF as well as freeze-pipe walls. Despite the differences in ΔT_{HTF}, the amount of energy extracted, E_{HEP}, is the same as observed in Fig. 8(c). It should be noted here that the HTF flow in the annulus is laminar in all scenarios; consequently, increasing the flow rate does not result in higher flow Nusselt number [48]. Thus, the amount of energy extracted is similar. Once the flow exceeds turbulence threshold, the Nusselt number will be affected by the flow rate which will increase the heat extraction capacity. Nonetheless, in laminar conditions considered in this study, η_l and η_g are similar at different laminar flow rates due to the similar energy extracted and stored in all scenarios.

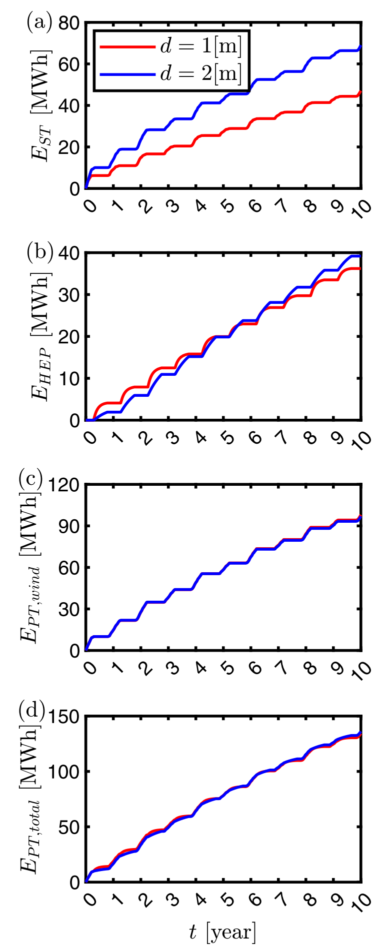

Fig. 12. Effect of d when the discharging period is six months: (a) Amount of cold-energy deposited by each ST in the CES pool, (b) amount of cold energy extracted by each HEP, (c) amount of energy extracted by each PT passively from available cold wind, and (d) total amount of energy extracted by each PT.

3.2.3. Effect of HTF inlet temperature

In field scenarios, the inlet temperature of the HTF is controlled by the amount of heat gained by the HTF at the PT. In this subsection, we aim at understanding how the HTF inlet temperature affects the efficiency of the CES system. As can be observed from Fig. 9, increasing

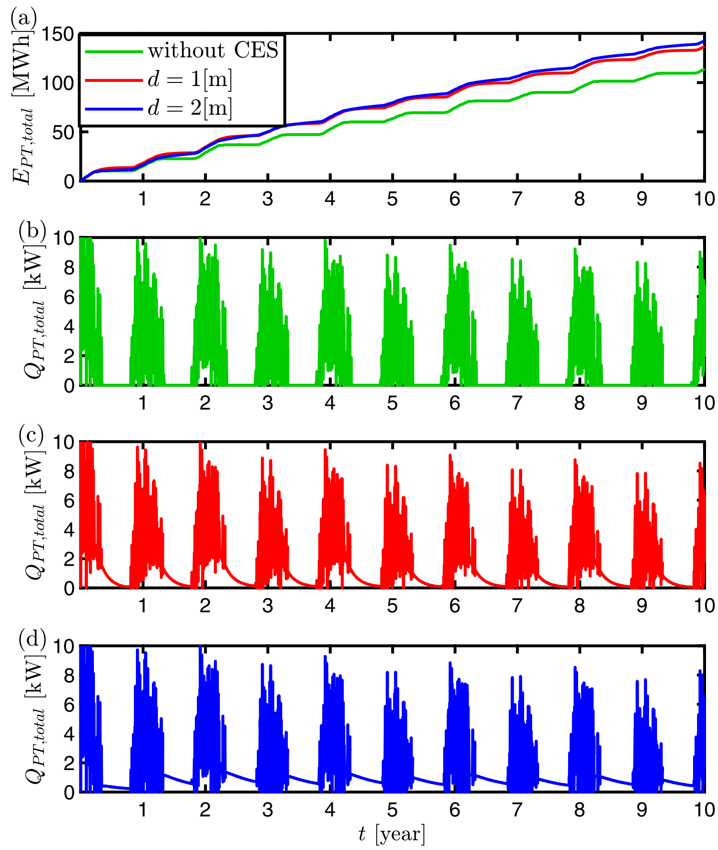

Fig. 13. Effect of integrating a CES system: (a) total energy extracted by each PT, (b) heat rate extracted by each PT without CES, (c) heat rate extracted by each PT when $d = 1$ [m], and (d) heat rate extracted by each PT when $d = 2$ [m].

the inlet HTF temperature linearly increases the system efficiency. At higher inlet temperatures, more energy can be extracted as deduced from Eq. (17). Further, higher inlet temperature can initiate energy extraction earlier than lower ones. For instance, when the inlet temperature is set at -1[°C], cold energy extraction starts from the first summer. Nevertheless, at inlet temperatures of -3[°C] and -5[°C], two winters are needed to charge the ground with sufficient cold energy so ground temperature of the wall is lower than the HTF inlet temperature.

3.3. Giant mine coupling with CES

In this section, the CES pool is coupled with the ground freezing process at the GMRP. First, the effect of spacing in the CES system and discharging period on the heat extraction capacity of PTs is examined. Particularly, $d = 1$ [m] and $d = 2$ [m] are considered due to the lower CES efficiency at higher d as observed in the previous subsection. Lastly, the potential advantage of utilizing a CES system is discussed by comparing it with a passive system without CES. In this subsection, the volume flow rate of the HTF is set at 1 [m^3/h]. Also, T_{in} (HTF inlet temperature to HEP) and T_{out} (HTF outlet temperature from HEP) are now coupled with PT. In other words, T_{in} equals to the outlet temperature of the HTF from the PT calculated using energy balance. Further, the inlet temperature of the HTF to the PT equals to T_{out}.

3.3.1. Analysis on the CES discharging period & spacing

In this subsection, the capability of the CES system to provide cold energy to PTs is examined by operating discharging period for four and six months. The impact of the spacing between STs and HEPs is also considered in the analysis.

First, a cold energy discharging period is set at four months to test the capability of the CES system to provide cold energy for short periods. When $d = 1$ [m], ΔT_{HTF} (with respect to the CES system) is higher than that of $d = 2$ [m] at the start of each discharging period, as can be seen from Fig. 10(a). This is attributed to the lower local temperature near the HEP at lower d. However, as the local cold energy is consumed, higher ΔT_{HTF} is noted when $d = 2$ [m] because of the larger amount of cold energy stored. The only exception is the first year due to the longer period needed for the cold energy to travel from the STs to the HEPs, as discussed in Section 3.2.1. The differences of the HTF temperature profile is reflected on the heat-rate transferred during warm seasons by HEPs, as shown in Fig. 10(b). As for the PTs, the heat-rate fluctuates significantly when heat is extracted during cold seasons due to the hourly variation of wind temperature and speed as per Fig. 4. However, It can be noted that the discharging period has the capacity to be extended for more than four months as the PTs are idle for around two months after each discharging period.

When increasing the discharging period to six months, a similar trend is observed in regards to ΔT_{HTF} and Q_{HEP} with few exceptions. Since the discharging period is now longer, the case of $d = 2$ [m] can provide higher power for longer periods especially after the third year due to the higher amount of energy stored, as shown in Figs. 11 and 12(a). Specifically, the amount of cold energy transferred is initially higher at $d = 1$ [m] for the first two years. After that, energy transferred at $d = 2$ [m] catches up and becomes slightly higher in a 10 year period, as can be seen in Fig. 12(b). This however does not result in a substantial increase in E_{PT} over a 10 year period, as observed in Fig. 12(d) due to the relatively high wind heat extraction of PTs during cold seasons, as can be seen from Fig. 12(c). In the longer run after ten years, it is expected that a CES spacing of two meters to have a larger impact.

3.3.2. Comparison with a traditional system

This study is concluded by highlighting the potential advantage of using a CES system. In Section 3.3.1, a longer discharging period only

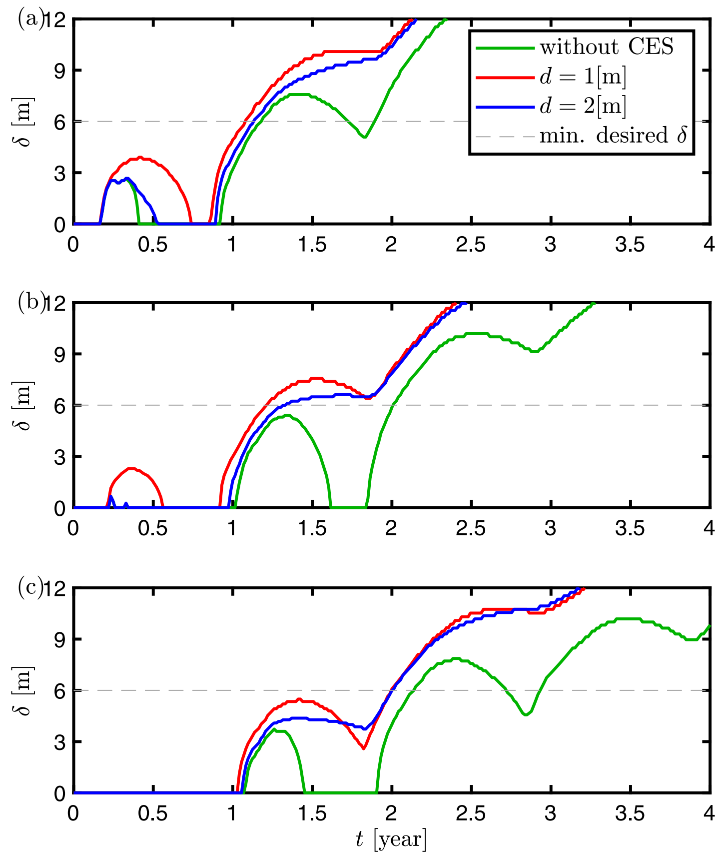

Fig. 14. Effect of integrating a CES system on the lateral frozen ground thickness at a depth of (a) 20 m (5 m above the contaminated chambers), (b) 50 m (middle of the contaminated chambers), and (c) 80 m (5 m below the contaminated chambers).

enhanced the performance of the overall system. Accordingly, in this section, HEPs are operated whenever the air temperature is too warm to run PTs, thus preventing PTs from becoming idle. In other words, energy stored in the CES pool is utilized whenever the air temperature is higher than the monitored evaporator temperature of the PT.

As can be seen from Fig. 13(a), the total energy extracted by a CES integrated PT is around 15% higher than a traditional thermosyphon without a storage system. Thus, the potential of a CES system to increase the efficiency of AGF applications is demonstrated, which is the main scope of this study proposing the concept of CES in AGF. The main evident difference between the two systems is the long idle period of a traditional thermosyphon with CES during warms seasons, as can noted in Fig. 13(b). Traditional thermosyphons remain idle for around 6 months a year, whereas our proposed system with integrated CES pool allow the thermosyphon to run year-round. In the first two years, it is observed that a CES system with $d = 1$ [m] performs better than that of a CES system with $d = 2$ [m]. Afterwards, the amount of energy extracted by PTs becomes larger when $d = 2$ [m], as discussed in the previous sections.

The increased energy extracted by adding a CES system also increases the extent of the frozen ground throughout the depth of the PTs, as shown in Fig. 14. Typically, a lateral frozen ground thickness of six meters is often desired between two PTs to ensure the availability of an impenetrable frozen body. At the top of the chambers, the six-meters limit is reached within 1.2 years in all scenarios, at different d or without a CES system, as can be seen in Fig. 14(a). However, as traditional thermosyphons without CES become dormant during warm seasons, the ground thaws below the six-meters threshold after 1.8 years. At deeper levels of the thermosyphon, the freezing time becomes larger due to the geothermal temperature gradient (see Eq. (18)). At the middle of the chambers (depth of 50 m), the six-meters limit is permanently maintained after 1.3 years when a CES system is employed. Nevertheless, the frozen ground formed by a traditional system thaws in the summer of the second year; a continuous six-meters δ is only formed after 2 years of operation. At the bottom of the chambers, the freezing time needed with a CES pool is around 1.9 years, as compared to 2.9 years without a CES system. Overall, the effect of integrating a CES pool is evident on decreasing the freezing time. Once the ground freezing process is completed, the CES pool can then be employed in various applications, such as heating of buildings or geothermal power generation.

4. Conclusion

In this study, a novel ground coupled cold energy storage (CES) concept is proposed for application of artificial ground freezing (AGF) and permafrost protection applications in cold regions. The proposed system is based on traditional passive thermosyphons supported by a CES pool that runs passive thermosyphons during warm seasons. The CES pool is made up of cold-energy storage thermosyphons (ST) and heat extraction pipes installed in the ground nearby the primary thermosyphons (PTs) operating in the site of interest. In cold seasons, while the PTs extract energy using naturally available cold wind, STs also utilize the cold wind to store cold energy. In warm seasons, HEPs transfer this cold energy to the primary thermosyphons (PT) operating on the site of interest, which is the Giant Mine in the present study. The proposed concept has been demonstrated by a well-validated numerical model.

In the results section, the effect of three parameters on the capacity and efficiency of the CES system is firstly investigated: (1) Spacing between STs and HEPs in the CES pool (d), (2) volume flow rate of the heat transfer fluid (HTF) in the HEP, and (3) inlet temperature of the HTF. The results reveal that there is an optimum spacing that yield in maximum cold energy extracted at each year of operation; shorter *d* is preferable in the short term and vice versa. Further, the volume flow rate of the HTF has negligible effect when the flow is laminar. Additionally, The inlet HTF temperature is linearly proportional to the CES efficiency.

Lastly, the CES system is coupled to the PTs for the case of the Giant Mine Remediation Project (GMRP). Our proposed system demonstrated an increase in the heat extraction of PTs by more than 15% as compared with a traditional system (without a CES). Accordingly the freezing process is completed one year faster with a CES system. As compared with hybrid thermosyphons that employ active mechanical refrigeration plants, the proposed concept saves 2.3 [GWh] and corresponding greenhouse gas emissions for every 100 thermosyphons.

In our future work, optimization analysis will be conducted to investigate the impact of several operational parameters, such as the discharging duration of cold energy, the CES layout & number of units.

CRediT authorship contribution statement

Ahmad F. Zueter: Methodology, Software, Validation, Formal analysis, Investigation, Data curation, Writing – original draft, Visualization. **Agus P. Sasmito:** Conceptualization, Investigation, Resources, Writing – review & editing, Supervision, Project administration, Funding acquisition.

Declaration of competing interest

The authors declare that they have no known competing financial interests or personal relationships that could have appeared to influence the work reported in this paper.

Acknowledgements

The authors would like to thank the FRQNT Development Durable du Secteur Minier – II (2020-MN-284402) and Ultra Deep Mining Network (UDMN) (241695 Tri-Council (NCE – UDMN) 2-003). The first author wishes to thank the McGill Engineering Doctoral Award (MEDA) and the FRQNT Doctoral award (Grant No. 2021-B2X-306519),

References

[1] Government of Canada, History of giant Mine, 2018, https://www.aadnc-aandc.gc.ca/.
[2] R. Silke, The Operational History of Mines in the Northwest Territories, Canada, Tech. rep., Yellowknife, 2009.
[3] Canada North Environmental Services, Giant Mine Human Health and, Tech. rep., 2018.
[4] H. Paulson, New study shows low risk to public health 70 years after giant Mine's toxic legacy, 2021, https://www.cbc.ca/.
[5] A.F. Zueter, G. Newman, A.P. Sasmito, Numerical study on the cooling characteristics of hybrid thermosyphons: Case study of the giant Mine, Canada, Cold Reg. Sci. & Technol. 189 (February) (2021) 103313, http://dx.doi.org/10.1016/j.coldregions.2021.103313.
[6] Environment and Climate Change Canada, Canada Emission Factors for Grid Electricity, Tech. rep., 2019, https://bullfrogpower.com.
[7] I. Holubec, Flat Loop Thermosyphon Foundations in Warm Permafrost, Tech. rep., I. Holubec Consulting Inc. Northwest Territories, 2008.
[8] E. Yarmak, E.L. Long, Recent developments in thermosyphon technology, in: Cold Regions Engineering: Cold Regions Impacts on Transportation and Infrastructure, Anchorage, 2002, pp. 656–662.
[9] J.W. Rooney, C.H. Riddle, R.L. Scher, Foundation rehabilitation at ADOT/PF jim river maintenance camp, in: Society of Petroleum Engineers - Arctic Technology Conference 2011e, Anchorage, 1991, pp. 829–840, http://dx.doi.org/10.2523/22226-ms.
[10] L. Guo, Z. Zhang, X. Wang, Q. Yu, Y. You, C. Yuan, Y. Xie, T. Gou, Stability analysis of transmission tower foundations in permafrost equipped with thermosiphons and vegetation cover on the Qinghai-Tibet Plateau, Int. J. Heat Mass Transfer 121 (2018) 367–376, http://dx.doi.org/10.1016/j.ijheatmasstransfer.2018.01.009.
[11] L. Xu, Y. Shen, L. Zhang, Study on stability of low embankment of the high temperature permafrost in Qinghai-Tibet railway, in: International Conference on Railway Engineering, 2004.
[12] S.P. Varlamov, Thermal monitoring of railway subgrade in a region of ice-rich permafrost, Yakutia, Russia, Cold Reg. Sci. & Technol. 155 (2018) 184–192.
[13] Q.Y. Zhu, W. Wang, S.Y. Wang, X.F. Zhou, G.Y. Liao, S.J. Wang, J.B. Chen, Unilateral heat-transfer asphalt pavement for permafrost protection, Cold Reg. Sci. & Technol. 71 (2012) 129–138.
[14] Y. Zhong, T. Ma, X. Huang, Asphalt mixture design and thermology experiments on heat-resistant surfaces in permafrost regions, J. Test. Eval. 43 (4) (2015) 833–840.
[15] W. Pei, M. Zhang, Z. Yan, S. Li, Y. Lai, Numerical evaluation of the cooling performance of a composite L-shaped two-phase closed thermosyphon (LTPCT) technique in permafrost regions, Sol. Energy 177 (November 2018) (2019) 22–31.
[16] M. Zhang, Y. Lai, Q. Wu, Q. Yu, T. Zhao, W. Pei, J. Zhang, A full-scale field experiment to evaluate the cooling performance of a novel composite embankment in permafrost regions, Int. J. Heat Mass Transfer 95 (2016) 1047–1056, http://dx.doi.org/10.1016/j.ijheatmasstransfer.2015.12.067.
[17] W. Ma, Z. Wen, Y. Sheng, Q. Wu, D. Wang, W. Feng, Remedying embankment thaw settlement in a warm permafrost region with thermosyphons and crushed rock revetment, Can. Geotech. J. 49 (9) (2012) 1005–1014, http://dx.doi.org/10.1139/T2012-058.
[18] Q. Ma, X. Luo, J. Gao, W. Sun, Y. Li, T. Lan, Numerical evaluation for cooling performance of a composite measure on expressway embankment with shady and Sunny slopes in permafrost regions, Energy (2022) 123194.
[19] A.L. Lyazgin, R.M. Bayasan, S.A. Chisnik, V.G. Cheverev, G.P. Pustovoit, Stabilization of pile foundations subjected to frost heave and in thawing permafrost, in: Eighth International Conference on Permafrostth International Conference on Permafrost, Zurich, 2003, pp. 21–25.
[20] R.M. Bayasan, A.G. Korotchenko, N.G. Volkov, G.P. Pustovoit, A.D. Lobanov, Use of two-phase heat pipes with the enlarged heat-exchange surface for thermal stabilization of permafrost soils at the bases of structures, Appl. Therm. Eng. 28 (4) (2008) 274–277, http://dx.doi.org/10.1016/j.applthermaleng.2006.02.022.
[21] Y. Zhang, K. Han, B. Xu, Z. Chang, Experimental study on the temperature evenness of heat pipe using magnetic nano-fluids as the working medium in permafrost regions, Adv. Mater. Res. 614–615 (2013) 327–330, http://dx.doi.org/10.4028/www.scientific.net/AMR.614-615.327.
[22] A.B. Solomon, A.M.R. Kumar, K. Ramachandran, B.C. Pillai, C.S. Kumar, M. Sharifpur, J.P. Meyer, Characterisation of a grooved heat pipe with an anodised surface, Heat Mass Transf. 53 (3) (2017) 753–763, http://dx.doi.org/10.1007/s00231-016-1856-8.
[23] Y. Tian, Z. Yang, Y. Liu, X. Cai, Y. Shen, Long-term thermal stability and settlement of heat pipe-protected highway embankment in warm permafrost regions, Eng. Geol. 292 (2021) 106269.
[24] V.K. Kukkapalli, J.H. Kim, S. Kim, Optimum design of thermosyphon evaporators for roadway embankment stabilization in the arctic regions, J. Mech. Sci. Technol. 35 (10) (2021) 4757–4764, http://dx.doi.org/10.1007/s12206-021-0941-1.
[25] V. Kukkapalli, S. Kim, Roadway embankment stabilization on permafrost using thermosyphons with Y-shaped evaporators, IOP Conf. Ser. Mater. Sci. Eng. 507 (1) (2022) http://dx.doi.org/10.1088/1757-899X/507/1/012017.
[26] W. Pei, M. Zhang, Y. Lai, X. Zhang, T. Luo, A self-adaption horizontal thermosyphon technology in uneven thermal control of roadway embankments in sub-arctic permafrost regions, Transp. Geotech. (2022) 100714.
[27] W. Pei, M. Zhang, S. Li, Y. Lai, L. Jin, W. Zhai, F. Yu, J. Lu, Geotemperature control performance of two-phase closed thermosyphons in the shady and sunny slopes of an embankment in a permafrost region, Appl. Therm. Eng. 112 (2017) 986–998.
[28] W. Pei, M. Zhang, Y. Lai, Z. Yan, S. Li, Evaluation of the ground heat control capacity of a novel air-L-shaped TPCT-ground (ALTG)cooling system in cold regions, Energy (2019) 655–668.
[29] Y. Chang, Y. Qihao, Y. Yanhui, G. Lei, Formation mechanism of longitudinal cracks in expressway embankments with inclined thermosyphons in warm and ice-rich permafrost regions, Appl. Therm. Eng. 133 (2018) 21–32.
[30] J. Chen, B. Zhang, R. Song, X. Dong, L. Zhang, C. Ji, Z. Bo, S. Ruifang, D. Xianfu, Z. Luxin, Observation study on the stability of frozen soil roadbed equipped with thermosyphon in chaidaer-muli railway, in: J. Zhao (Ed.), Advanced Materials Research, in: Vol. 255-260 of Advanced Materials Research, Kunming Univ Sci & Technol; Int Assoc Sci & High Technol, 2011, pp. 4003–4007.
[31] A.M. Wagner, Creation of an artificial frozen barrier using hybrid thermosyphons, Cold Reg. Sci. & Technol. 96 (2013) 108–116.
[32] D.F. Haynes, J.P. Zarling, W.F. Quinn, G.E. Gooch, Laboratory tests with a hybrid thermosyphon, in: Proceedings of the 10th International Conference on Ocean, Offshore and Arctic Engineering, Vol. 4, American Society of Mechanical Engineers, Stavanger, 1991, pp. 93–99.
[33] A.M. Wagner, J.B. Maakestad, E. Yarmak, T.A. Douglas, Artificial ground freezing using solar-powered thermosyphons.
[34] M. Alzoubi, S. Ali Ghoreishi-Madiseh, A.P. Sasmito, N. Kunz, A. Guimaraes, Renewable energy-based artificial ground freezing as an adaptation solution for sustainability of permafrost in post-climate change conditions, IOP Conf. Ser. Earth Environ. Sci. 268 (1).
[35] M.A. Alzoubi, S. Poncet, A.P. Sasmito, Hybrid artificial ground freezing as a sustainable solution for containing hazardous-waste in critical environmental projects, Cold Reg. Sci. & Technol. 192, 103401.

[36] W. Pei, M. Zhang, S. Li, Y. Lai, Y. Dong, L. Jin, Laboratory investigation of the efficiency optimization of an inclined two-phase closed thermosyphon in ambient cool energy utilization, Renew. Energy 133 (2019) 1178–1187.
[37] M. Kaviany, Principles of Heat Transfer in Porous Media, Springer Science & Business Media, 2012.
[38] A. Zueter, A. Nie-Rouquette, M.A. Alzoubi, A.P. Sasmito, Thermal and hydraulic analysis of selective artificial ground freezing using air insulation: Experiment and modeling, Comput. Geotech. 120 (2020) 103416.
[39] Y.A. Cengel, Heat and Mass Transfer: Fundamentals and Applications, third ed., McGraw-Hill, Boston, 2007.
[40] A.F. Zueter, M.S. Tareen, Newman G., A.P. Sasmito, Dynamic cfd modeling coupled with heterogeneous boiling for deep two phase closed thermosyphons in artificial ground freezing, Int. J. Heat Mass Transfer 203 (2023) 123781.
[41] H. Imura, H. Kusuda, J.-I. Ogata, T. Miyazaki, N. Sakamoto, Heat transfer in two-phase closed-type thermosyphons, JSME Trans. 45 (1979) 712–722.
[42] W. Nusselt, The condensation of steam on cooled surfaces, Z. Ver. Dtsch. Ing. 60 (1916) 541–546.
[43] A. Zukauskas, Heat transfer from tubes in crossflow, in: Advances in Heat Transfer, Vol.8, Elsevier, 1972, pp. 93–160.
[44] K.A. Gardner, Efficiency of extended surface, Trans. ASME 67 (1945) 621–631.
[45] B.K. Hardik, P.K. Baburajan, S.V. Prabhu, Local heat transfer coefficient in helical coils with single phase flow, Int. J. Heat Mass Transfer 89 (2015) 522–538.
[46] R.A. Seban, E.F. McLaughlin, Heat transfer in tube coils with laminar and turbulent flow, Int. J. Heat Mass Transfer 6 (5) (1963) 387–395.
[47] C.M. White, Streamline flow through curved pipes, Proc. R. Soc. London. Ser. A Contain. Pap. A Math. Phys. Character 123 (792) (1929) 645–663.
[48] R. Shah, A. London, Concentric annular ducts, in: Laminar Flow Forced Convection in Ducts, Academic Press, New York, 1978, pp. 284–321, Ch. XII.
[49] A.F. Zueter, M. Xu, M.A. Alzoubi, A.P. Sasmito, Development of conjugate reduced-order models for selective artificial ground freezing: Thermal and computational analysis, Appl. Therm. Eng. 190 (2021) 116782.
[50] A.F. Zueter, A.G. Madiseh, F.P. Hassani, A.P. Sasmito, Effect of freeze pipe eccentricity in selective artificial ground freezing applications, ASME J. Therm. Sci. Eng. Appl. 14 (2022) 011015.
[51] A.F. Zueter, S. Akhtar, A.P. Sasmito, Uncertainty analysis of operational conditions in selective artificial ground freezing applications, J. Sustain. Min. 21 (3) (2022) 169–179.
[52] Government of Canada, Historical data, 2019, https://climate.weather.gc.ca/.
[53] National Institute of Standards and Technology, NIST chemistry webbook, 2018, https://webbook.nist.gov/.
[54] SRK Consulting (Canada) Inc., Freeze Optimization Study Update for MVEIRB and Parties Aboriginal Affairs and Northern Development Freeze Optimization Study Update for MVEIRB and Parties, Tech. Rep., 2012, August, Ottawa.
[55] P.H. Agson-Gani, A.F. Zueter, M. Xu, S.A. Ghoreishi-Madiseh, J.C. Kurnia, A.P. Sasmito, Thermal and hydraulic analysis of a novel double-pipe geothermal heat exchanger with a controlled fractured zone at the well bottom, Appl. Energy 310 (2022) 118407, http://dx.doi.org/10.1016/j.apenergy.2021.118407.
[56] S. Pokhrel, L. Amiri, A. Zueter, S. Poncet, F.P. Hassani, A.P. Sasmito, S.A. Ghoreishi-Madiseh, Thermal performance evaluation of integrated solar-geothermal system; A semi-conjugate reduced order numerical model, Appl. Energy 303 (2021) 1–16.